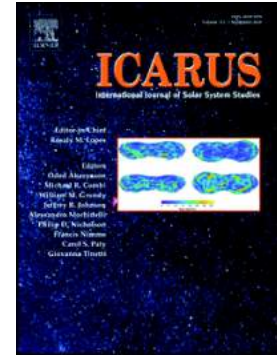


Closed depressions in Kotido crater, Arabia Terra, Mars. Possible evidence of evaporite dissolution-induced subsidence

Carlotta Parenti, Francisco Gutiérrez, Davide Baioni, Ángel García-Arnay, Jorge Sevil, Erica Luzzi



PII: S0019-1035(20)30071-3

DOI: <https://doi.org/10.1016/j.icarus.2020.113680>

Reference: YICAR 113680

To appear in: *Icarus*

Received date: 17 May 2019

Revised date: 15 January 2020

Accepted date: 28 January 2020

Please cite this article as: C. Parenti, F. Gutiérrez, D. Baioni, et al., Closed depressions in Kotido crater, Arabia Terra, Mars. Possible evidence of evaporite dissolution-induced subsidence, *Icarus*(2020), <https://doi.org/10.1016/j.icarus.2020.113680>

This is a PDF file of an article that has undergone enhancements after acceptance, such as the addition of a cover page and metadata, and formatting for readability, but it is not yet the definitive version of record. This version will undergo additional copyediting, typesetting and review before it is published in its final form, but we are providing this version to give early visibility of the article. Please note that, during the production process, errors may be discovered which could affect the content, and all legal disclaimers that apply to the journal pertain.

Closed depressions in Kotido Crater, Arabia Terra, Mars. Possible evidence of evaporite dissolution-induced subsidence

Carlotta Parenti (1), Francisco Gutiérrez (2)*, Davide Baioni (3), Ángel García-Arnay (2), Jorge Sevil (2), Erica Luzzi, E. (4)

(1) Dipartimento di Scienze Chimiche e Geologiche, Università degli Studi di Modena e Reggio Emilia, Italy

(2) Departamento de Ciencias de la Tierra, Universidad de Zaragoza, Spain

(3) Dipartimento di Scienze Pure e Applicate, Università degli Studi di Urbino Carlo Bo, Italy

(4) Department of Physics and Earth Sciences, Jacobs University Bremen, Germany

* Corresponding author: fgutier@unizar.es; Edificio Geológicas; Pedro Cerbuna 12; 50009 Zaragoza, Spain

Abstract

The identification of karst sinkholes in Mars may provide evidence of dissolution processes caused by liquid water and information on paleoclimatic and paleohydrological conditions. This work presents a comprehensive cartographic inventory of 513 closed depressions developed on evaporite-bearing Equatorial Layered Deposits (ELDs) within Kotido crater, Arabia Terra. Detailed mapping, morphometric analyses and spatial distribution relationships reveal a number of features supporting that the depressions correspond to collapse sinkholes related to evaporite dissolution: (1) suitable topographic and litho-structural conditions for the development of a fracture-controlled epigene evaporite karst; (2) presence of open fissures at the foot of the scarp margins; (3) dimensions and frequency-size distributions comparable with those reported on Earth; (4) spatial association with high-permeability zones (i.e., fractures). Some characteristics of the depressions indicate that they have been re-shaped and enlarged by wind erosion: (1) dominant orientation consistent with the prevalent one-directional winds; (2) differing morphological characteristics on the downwind- and upwind-sides; and (3) nested depressions associated with the upwind sector. The relatively fresh appearance of the depressions and the lack of impact craters suggest a poorly constrained Amazonian karstification phase in the region.

Key words: Sinkholes; Evaporite karst; Aeolian erosion; Frequency-size relationships

1. Introduction

Unravelling the origin of closed depressions is frequently a challenging geomorphological problem, especially when subsurface data gathered by intrusive and/or non-intrusive methods is not available. The formation of closed depressions may be related to several genetic mechanisms acting individually or in combination (e.g., Waltham, 1989): (1) differential mechanical erosion of the ground surface (e.g., deflation basins); (2) lowering of the ground by preferential surface dissolution at specific locations (e.g., solution sinkholes); (3) accumulation of deposits with an irregular top surface (e.g., moraines, landslides, dunes); (4) explosive activity (e.g., explosion craters); (5) impact of a solid body (e.g., impact craters); and (6) subsidence due to mass and/or volume depletion in the subsurface (e.g., subsidence sinkholes, thermokarst depressions, collapse calderas, sinkholes related to lava tubes, compaction/consolidation-related depressions). Mechanisms 4, 5 and 6 involve the deformation of the ground and 4 and 5 are commonly accompanied by the ejection of material.

According to Johnson (2008), four basic conditions are required for evaporite karst development: (1) the presence of soluble evaporitic sediments; (2) a supply of liquid water unsaturated with respect to the evaporitic minerals; (3) an outlet whereby the solution (or brine) can escape; and (4) a gradient causing water to flow through the system. All these conditions can be found on Mars. The Martian surface contains soluble evaporite minerals in numerous regions, as demonstrated by data gathered with instruments of several missions (e.g., Bibring et al., 2006; Murchie et al., 2007). The presence of liquid water at the surface and in the subsurface has been widely demonstrated (e.g., Carr, 2012; Schon et al., 2012; García-Arnay et al., 2018). Suitable subsurface flow conditions can be assured by the presence of permeability features (e.g., fractures) and hydraulic gradients largely governed by the topography. In fact, a number of studies based on the analysis of high-resolution images propose the presence of karst landforms attributable to evaporite dissolution (Gindrod and Balme, 2010; Flahaut et al., 2015; Baioni, 2018 and references therein), notably sinkholes, which are widely regarded as the main diagnostic surface landform in karst areas (Ford and Williams, 2007). These geomorphic features are

postulated as useful lithological indicators, and valuable markers of past paleoclimatic and paleohydrological conditions since dissolution requires the presence of liquid water.

The existence of karst landforms and sinkholes have been hypothesized in many regions of Mars since the first images of the Viking Orbiter became available (Schaffer, 1990; Kargel et al., 2004; Preuschmann et al., 2006; Wyrick et al., 2004). The first account was probably published by Schaffer (1990), who noted three major localities in the northern plains of Mars (Arcadia Planitia, western Utopia Planitia, and eastern Acidalia Planitia) with “thumbprint” terrain riddled by depressions that could be related to differential solution of extensive carbonate deposits in low-lying areas. In a brief note, Smith et al. (2006) indicated that Mars hosts environments with evaporite sediments favourable for karst development and has a weaker gravitational field that should allow the formation of subsurface cavities larger than those occurring on Earth before their collapse. These authors, using low-resolution imagery identified a number of possible sinkholes in Kasei, Tiu and Simud Valles. Grindrod and Balme (2010) proposed a conceptual hydrogeological model for Hebes Chasma, whereby groundwater flow from the central elevated mound could discharge in the surrounding basin floor, leading to the crystallization of hydrated minerals, in which karst landforms including solution possible dolines have developed. A number of recent works based on high-resolution images provide strong evidence of the presence of sinkholes in Martian evaporite deposits (e.g. Baioni et al., 2009; Baioni and Wezel, 2010; Flahaut et al., 2015). Baioni and Sgavetti (2013) interpreted sinkholes related to evaporite dissolution in the northern Sinus Meridiani region, based on the presence of sulphates indicated by spectral analyses and the morphological and morphometric similarity of the depressions with sinkholes developed on Earth. These authors proposed that the observed variable degree of karst development could be related to variations in the solubility of different lithological units. Baioni and Tramontana (2015) documented putative sinkholes related to dissolution of sulphate-bearing layered deposits in Iani Chaos. Their interpretation was mainly based on the morphological analogy with terrestrial sinkholes and a discard analysis considering other potential genetic mechanisms. The authors suggested that the depressions record a single wet period, probably related to ice melting in the late Amazonian. Similar landforms have been documented in Meridiani Planum (Baioni, 2019), Tyrrhena Terra (Baioni and Tramontana, 2016), Coprates Chasma (Baioni et al., 2011), Tithonium Chasma (Baioni, 2013) and Juventae Chasma (Baioni and Tramontana, 2017). Large closed depressions of the order of kilometres or tens of kilometres long have been also attributed to dissolution-induced

subsidence. In an early work, Croft (1989) addressed the controversial origin of the numerous large-volume ($\geq 10^2 \text{ km}^3$) enclosed depressions (chasmata) associated with the canyons linked to Valles Marineris. The author advocated for a combined karst-tectonic model, involving both collapse induced by structurally controlled dissolution of carbonate rocks and extensional tectonics. Recently, Rodriguez et al. (2016) attributed the origin of the elongated enclosed depressions several tens of kilometres long of Noctis Labyrinthus to collapse processes. These authors explain the subsidence phenomenon by conduit development by structurally-controlled groundwater flow along salt-rich deposits, from the Tharsis volcanic rise towards Valles Marineris. In the bottom of one of the linear troughs of Noctis Labyrinthus, which is underlain by sulphate-bearing light-toned deposits, Baioni (2018) characterised shallow rimless pits mostly tens to hundreds of meters long. The author ascribed these depressions to a relict evaporite karst.

A number of works provide detailed descriptions of enclosed depressions on Mars attributable to the dissolution of evaporitic sediments, generally supported by some morphometric data and selected images. However, to our knowledge, such previous studies lack detailed cartographic inventories and comprehensive morphometric and spatial distribution analyses, which may contribute to infer more robust genetic interpretations. Additionally, most previous works analyse sinkholes individually, without considering their relationships with other landforms that may provide some clues on the origin and morphological evolution. In this work we present a cartographic inventory of closed depressions developed on evaporitic layered deposits in Kotido crater, Arabia Terra. The detailed map, including other features such as fractures and data on wind direction, has been used to extract and analyse morphometric parameters and the spatial distribution of the depressions. The morphometric analyses include the production of frequency-size relationships, which are compared with scaling relationships generated for karst sinkholes on Earth. The resulting qualitative and quantitative data provides the objective basis for discussing the origin and controlling factors of the depressions.

2. Study area

The study area is located in the east-central sector of Kotido crater (centered at 9.1°W , 1°N), situated in Arabia Terra (**Fig. 1**). This equatorial region, characterised by a gently sloping topography, represents a gradual transition between the highlands and lowlands of Mars, in contrast with the sharp dichotomy observed in other regions. The Kotido crater is

one of the many crater basins that hosts Equatorial Layered Deposits (ELDs). This is the informal term used to collectively designate the light-toned layered deposits found in a wide range of geomorphic settings within the equatorial regions of Mars (e.g., Okubo et al., 2009; Pondrelli et al., 2019). The stratigraphic distribution of the ELDs ranges from the Noachian-Hesperian transition to the lower Hesperian (e.g., Pondrelli et al., 2005), and according to spectral data they include monohydrated and/or polyhydrated sulphates (e.g., Gendrin et al., 2005; Bibring et al., 2006; Mangold et al., 2008). These sulphate-bearing sediments postdate Noachian argillaceous units and are thought to record a major environmental change in the history of Mars (Bibring et al., 2006).

The Kotido crater is a circular topographic basin 40 km across and around 1 km deep, from the rim to the floor. The substratum in which the Kotido crater was formed and that underlies the ELDs is formed by rocks of the “Middle Noachian highland unit” (mNh) (Tanaka et al., 2014). The ELDs correspond to the “Undivided etched unit” (HnMe_u) mapped by Hynek and Di Achille (2017) within the crater and in the nearby inter-crater plains. These authors indicate that the surfaces of unit HnMe_u are “tabular to rugged and intensely affected by aeolian erosion”. Pondrelli et al. (2019), using the equations of Garvin et al. (2003) and Robbins and Hynek (2013), reconstructed the original geometry of the crater, inferring a rough estimate for the thickness of its sedimentary fill of 1 km. Pondrelli et al. (2019) mapped the ELDs of Kotido crater at 1:20,000 scale, where they show significant variability and good exposure conditions with limited dust cover. They analysed their characteristics (i.e., morphology, texture, composition) and architectural features in order to infer the depositional environment and processes.

The ELDs exposed in Kotido crater consist of interbedded light- and dark-toned deposits, locally with interspersed intermediate-tone mounds (Pondrelli et al., 2019). The light-toned sediments are composed of well-stratified layers or packages of meter-scale thickness forming undulated surfaces. The dark-toned layers are made of more erodible material with smoother texture that tend to occur in topographically lower areas. The attitude of the ELDs of Kotido crater show spatial variations. In the central sector of the crater they mainly lie horizontally or show gentle dips, whereas in the marginal areas are affected by gentle folds.

Pondrelli et al. (2019) reported and illustrated the following morphological features in the layered deposits of Kotido crater: (1) Mounds in lateral continuity with the layered deposits, displaying a rounded depositional geometry, occasionally with an apical pit, and commonly forming alignments. (2) Straight to sinuous scarps, mesas, buttes and cuestas controlled by the more resistant horizontal or dipping light-toned beds, acting as caprocks. (3) Elongated yardangs with a prevalent NE trend generated by aeolian erosion. (4) Kilometre-scale linear layered ridges made up of resistant material and locally in spatial association with the mounds. These structurally controlled features are interpreted as fissure ridges formed by the upwelling of material through fractures or faults. According to Pondrelli et al. (2019), these lineaments show a roughly radial or circular distribution, suggesting that they are influenced by fracturing associated with the formation of the impact crater. (5) Numerous closed depressions that riddle the ELDs, which are the focus of this investigation. Regarding these depressions, Pondrelli et al. (2019) indicate that their “characteristics are comparable both in shape and size with dissolution-related morphologies typical, although not exclusive, of evaporite rocks. They also point that “aeolian erosion has been invoked to explain similar morphologies in the etched terrains of Arabia Terra. Pondrelli et al. (2019) interpret that the ELDs of Kotido crater were deposited in a playa-lake environment with spring mounds and fissure ridges fed by salt-rich pressurized groundwater. Sedimentation was characterised by alternating periods of evaporitic (light-toned layers) and fine-grained detrital sedimentation (dark-toned layers). They propose that the gentle dips and antiforms observed in the strata could be related to deposition over an inherited topography (i.e. sediments draping a paleorelief) or post-sedimentary deformation. A similar interpretation was proposed by Pondrelli et al. (2015) for the ELDs occurring inside and around the nearby Firsoff crater. Other authors relate ELDs occurring all over the region to deposition in groundwater discharge areas (Ori and Baliva, 1999; Malin and Edgett, 2000; Rossi et al., 2008; Oehler and Allen, 2008; Pondrelli et al., 2011; Franchi et al., 2014; Luzzi et al., 2018). Andrews-Hanna et al. (2010) proposed that oscillations of the regional groundwater table may have played an important role in the deposition of ELDs.

The ELDs in the mapped sector of Kotido crater are unconformably overlain by dark-toned dune fields, mainly concentrated in topographic lows, and slope deposits with distinctive rockfalls. The latter are typically associated with steep-slopes controlled by resistant light-

toned deposits (caprock), including the scarped margins of the closed depressions and residual reliefs.

3. Data and methodology

A sector within the floor of Kotido Crater, covering 21.7 km² and underlain by ELDs, was selected for investigating the closed depressions. This area includes numerous depressions with variable geomorphic features and is large enough to perform statistically significant analyses. The landforms were mapped and analysed in a GIS environment (ArcGIS 10.5.1) using the stereo-pair images ESP_016776_1810 and ESP_016921_1810 (0.5 m/pixel) from the High Resolution Imaging Science Experiment (HiRISE) instrument (McEwen et al., 2007) onboard NASA's Mars Reconnaissance Orbiter. A DEM was produced from these stereo pairs (~0.58 m in resolution) by means of ASP (Ames Stereo Pipeline, NASA). It was bundle adjusted to the global topography provided by the MOLA dataset and aligned to HRSC. Spatial data was projected on the coordinate system Mars2000 Equidistant Cylindrical. DEMS generated using the NASA ASP may include non-consistent elevation data along shadowed areas (e.g., inner part of the depression rims) because the stereo correlation in these zones does not capture clear distinctive boundaries easily matched between the stereo-pair images (Watters et al., 2017; Beyer et al., 2018). As a result, the DEM used in the cartographic analysis includes some no-data gaps in these areas, which can be observed in Figs. 1 and 3. Elevation data corresponding to these areas were interpolated in order to minimize their effect in the calculation of volume parameters.

Our mapping was mainly focused on the manual digitizing of the enclosed depressions on the HiRISE images. Automatic mapping using the DEM was discarded since these procedures tend to generate a high proportion of false positives and overlook numerous sinkholes (e.g., Doctor and Young, 2013; De Carvalho-Junior et al., 2014). Eventually, topographic profiles constructed with the DEM aided in the identification and precise mapping of the depression edges. The cartographic inventory includes simple depressions and compound basins resulting from the coalescence of several adjoining depressions. It excludes potential former closed depressions opened by erosion whose mapping would be highly subjective. The geomorphological map also contains other features that may shed some light into genetic processes and controlling factors such as dune fields and the inferred prevalent wind direction, and fractures (**Fig. 2**).

The map produced, together with the DEM, were used to extract morphometric parameters, analyse frequency-size relationships and perform spatial analyses. The following morphometric parameters were obtained for the depressions: major axis, orientation of major axis, area, elongation ratio, perimeter, circularity ratio, mean elevation of the perimeter, volume, elevation of deepest point and depth. Table 1 includes the definition of these parameters and the procedure used for their measurement. The approximate volume of the depressions was calculated with the polygon volume tool of ArcGIS following the procedure explained in Table 1. However, a null volume was obtained for 29 depressions (<6% of the inventory) of limited area (<550 m²), probably related to artefacts in the DEM and a small offset between the images used for mapping and the DEM. The volume of these depressions has been indirectly estimated using an exponential regression with a reasonable goodness of fit ($y=0.0012x^{1.8598}$; $R^2 = 0.689$) that relates the area of the sinkholes smaller than 5,000 m² and their volume. Table 2 includes maximum, minimum and average values of some of the parameters, as well as the standard deviation. Azimuth data was plotted on rose diagrams with the GeoRose software. The frequency-size relationships of the depressions have been analysed considering their major axis, area and volume and generating best-fit regression functions.

The spatial distribution analysis includes, in addition to qualitative observations, the production of density maps of depressions and fractures, the calculation of the nearest neighbour index (NNI) for the depressions, and the comparison of rose diagrams generated with the orientation of the depressions, fractures and wind direction. Two types of sinkhole density models were generated computing the number of depressions and the proportion of the area occupied by depressions within a search radius. The density model by number was generated with the centroids of the depressions (Feature to Point tool) and applying a uniform Kernel function (Kernel Density tool). The areal density map was generated transforming the depression polygons into raster and then into points (Polygon to Raster and Raster to Point tools) and applying a uniform Kernel function (Kernel Density tool). In both cases, the default search radius was used, calculated specifically to the input dataset using a spatial variant of Silverman's Rule of Thumb that is robust to spatial outliers (i.e., points far away from the rest) (Silverman, 1986). The NNI of the depressions was calculated with their centroids with the Average Nearest Neighbour tool to quantify dispersion versus clustering.

4. Results

4.1. General features and morphometric parameters

The general topography in the investigated sector of Kotido crater is characterized by undulating erosional plains, riddled by numerous closed depressions and locally interrupted by residual reliefs (**Fig. 3**). The elevation ranges from -3,079 m to -2,850 m, and its mean elevation is situated around 120 m above the deepest point of the crater floor. The area is underlain by ELDs, showing an alternation of resistant light-toned beds and more erodible dark-toned units. Locally, this stratified material shows gentle dips and open folds. The residual reliefs include prominent steep-sided mesas and buttes capped by resistant beds, as well as some NE-oriented elongated hills with well-defined crests attributable to yardangs (Pondrelli et al., 2019).

The mapped closed depressions show a wide range of morphologies and dimensions. The major axis ranges from 8 m to 342 m (average 55 m) and the area from 44 m² to 29,371 m² (average 1,615 m²) (**Table 2**). Some depressions show a subcircular morphology in plan view, however, a significant proportion of them have an elongated shape (**Fig. 3**). Around 48% and 21% of the depressions have elongation ratios lower than 0.7 and 0.6, respectively. The orientation of the major axis of the depressions show a broad NE prevalent trend; N20-80E (**Fig. 4A**). The edges of most of the depressions show a continuous trace, whereas some show a rather irregular outline. The perimeter of the depressions varies from 24 m to 1,248 m (average 149 m), and the mean circularity ratio is 0.71, with values as low as 0.22 for the depressions with irregular edges (**Table 2**).

The closed depressions commonly display well-defined scarped edges controlled by resistant light-toned layers. These caprocks form free-face scarps, whereas the underlying more erodible material is generally covered by slope deposits (debris slopes), including distinctive rock-falls. Other depressions have prominent ridge-like edges or poorly defined boundaries (**Fig. 3A, B**). The floor of the depressions tends to be mantled by dark-toned deposits, mostly dunes, which locally overlap the edges of the depressions. In addition, planar bedrock outcrops occur in the bottom of the depressions. The NE-oriented

elongated depressions typically display different morphological features on the opposite ends. The SW edges tend to be sharper and steeper, whereas the NE edges show gentler slopes, seldom with vaguely-defined boundaries. Moreover, the outline of these NE sides tends to be more irregular (**Fig. 3A, B, C**). Some depressions show a tear-drop morphology, with a subcircular shape interrupted on the NE side by an outward projection (**Fig. 3A**). The area also includes depressions with smaller nested depressions, typically associated with the SW portion of the larger basin (**Fig. 3D**).

The depressions are rather shallow with maximum and average depths of 12 m and 2.8 m, respectively. The volume of the depressions, roughly estimated with the DEM, reaches 124,51 m³, with an average of 3,149 m³. The whole set of inventoried depressions has an aggregate volume of 1,615,650 m³. This value, together with the area of the mapped zone (21,725,412 m²), yields an average lowering of the ground surface by depression-forming processes of 7.4 cm.

Several depressions show wide-open arcuate fissures along the foot of the scarp edge, with the inner block apparently tilted (toppled) towards the centre of the basin. These features are commonly observed on the western and southwestern edge of the depressions (**Fig. 3E, F**). Depressions and depression alignments are frequently associated with fractures (**Fig. 3B, C**). The latter may have a variable expression: (1) low-relief ridges indicative of more resistant material; (2) darker tone lineaments without topographic expression; and (3) linear scarps attributable to differential erosion and/or dip-slip fault displacement.

4.2 Frequency-size relationships

The frequency-size distribution of the 513 mapped depressions has been analyzed plotting various morphometric parameters in logarithmic scale (Ma: major axis; A: area; V: volume) against cumulative frequency (Fc; proportion of depressions equal or larger than a given size value) (**Fig. 5**). The empirical data show a general linear trend in the semi-log graph that can be fitted with a high goodness of fit with logarithmic functions. A higher correlation coefficient is obtained for the major axis and the area (R^2 : 0.96) than for the volume (R^2 : 0.94), which was measured with significantly lower accuracy, especially for the small depressions (**Table 1**). The major axis, area and volume data range cover 1.6, 2.8 and 7.5 orders of magnitude, respectively, given by log (maximum value / minimum value) (**Table**

2). The empirical major axis and area data show a slight deviation from the fitted regressions for the extreme-size values of the distribution (upper and lower cut-offs or truncations). The adjusted relationships predict higher cumulative frequency for the small depressions and lower cumulative frequency for the largest ones. These truncations affect to a larger size range for the volume data, particularly for the small-volume depressions that include outliers. It should be noted that the volume of some of the smaller depressions was indirectly estimated with a regression that relates the area and the volume of the depressions.

4.3 Spatial distribution analysis

The relative spatial distribution of the mapped sinkholes can be analyzed through the nearest neighbour index (NNI; see formulation in **Table 1**). This index, extensively used for the characterization of sinkholes (Gutiérrez, 2016 and references therein), quantifies the degree of clustering versus dispersion of features distributed within a particular area and varies from 0 to 2.15 (Clark and Evans, 1954; Williams, 1972). A NNI equal to 2.15 indicates maximum dispersion with uniform hexagonal pattern, 1 indicates perfect random distribution and 0 indicates maximum clustering (virtual sinkhole field in which the centroids of all sinkholes are attached to another). A NNI of 0.82 has been calculated for the study area, with a z-score of -7.52 and a p-value of 0.0. This index indicates an overall random distribution with some clustering. Visual inspection of the geomorphological map reveals that the depressions show a clear clustered pattern in some sectors, whereas in other zones sinkholes are very scarce and show a more dispersed distribution (**Fig. 2**). These patterns can be analyzed through the production of sinkhole density models.

A total of 513 sinkholes have been mapped in an area covering 21.7 km², yielding a density of 23.6 depressions/km². Baioni (2018) estimated a density of 10.4 depressions/km² in a putative evaporite karst area of Western Noctis Labrinthus. The value obtained in Kotido crater is probably biased by the selection of a sector with a high number of closed depressions. The inventoried closed depressions, with an aggregate area of 0.83 km², have an areal density of 3.8%. Note that this is the percentage of the area covered by closed depressions, and excludes open former enclosed depressions. The spatially-distributed density models of depressions by number and area show very similar patterns (**Fig. 6A, B**). These maps highlight the areas with higher number of depressions or depression coverage, and their comparison allow identifying zones with

few but large sinkholes or with many but small depressions. Both models, as well as the geomorphological map, show an uneven sinkhole distribution, with similar areas characterized by high density by number (>34 depressions/km²) and area ($>23\%$), and relatively large zones with very low density (<8 depressions/km² and $<2\%$). Grossly, the high density zones include a NNE oriented belt located in the NW half of the study area and a shorter NW-SE oriented band in the SE quadrant.

A total of 1341 fractures have been mapped, ranging in length from 4.7 to 835 m, and with an average length of 46.7 m (**Fig. 2**). The orientation of the fractures shows a clear unimodal distribution, with a preferred NNE-SSW trend; N10-50E (**Fig. 4B**). A Kernel fracture density model, which expresses the number of fractures by area, shows some high fracture density zones in the northern and western sectors (>6.98 fractures/km²) of the study area and a very low density zone in the SE quadrant (<0.96 fractures/km²) (**Fig. 6C**). The comparison of the density models of depressions and fractures indicate both some spatial correlation in the NE half of the study area and the opposite in the SE quadrant, with high depression density and very low fracture density.

A total of 250 dune fields have been mapped in the study area (not shown in the geomorphological map). The wind direction has been inferred for each of them on the basis of the orientation of the crest of transverse dunes and the position of the steeper downwind side of the dunes (**Figs. 2, 4C**). The distribution of the wind vectors shows a well-defined ENE-directed wind (N60-80E).

5. Discussion

The cartographic, morphometric and spatial distribution analyses carried out with the 513 depressions inventoried in the selected zone of Kotido crater, covering 21.7 km², provide a comprehensive basis for the characterisation of these landforms associated with ELDs, and for discussing their potential origin. Several lines of evidence concurrently point to evaporite-dissolution subsidence as a likely genetic mechanism, which entails subsurface dissolution by liquid water and subsidence of the overlying undermined sediments (Waltham et al., 2005; Gutiérrez and Cooper, 2013; Gutiérrez et al., 2014):

- Spectral data indicate that the ELDs include soluble hydrated sulphates (Gendrin et al., 2005; Bibring et al., 2006; Mangold et al., 2008). Consistently, the layered deposits of Kotido crater have been interpreted as evaporitic sediments formed in a playa-lake environment fed by salt-rich groundwater rising from a confined aquifer (artesian flow), preferentially along fractures (Pondrelli et al., 2019). These data strongly suggest that the area is underlain by a suitable substratum for the development of karts features; i.e., fractured evaporites.
- Some depressions display open fissures along the foot of the scarped edges, with the downthrown side apparently toppled towards the centre of the depression (**Fig. 3E, F**). These surface ruptures provide evidence of ground deformation related to mass depletion in the subsurface, attributable to the development of dissolution cavities and the collapse of the roof material. These extensional fissures are commonly found along the edge of the bottom of collapse sinkholes developed in karst rocks, and especially in evaporites, characterised by a more ductile rheology. The evaporitic sediments underlain by a cavity tend to bend downwards (sagging), experiencing centripetal contraction. The radial shortening is counterbalanced by the development of annular extensional fissures at the margins associated with the collapse ring faults (e.g., Gutiérrez et al., 2008; Gutiérrez, 2016). **Figure 7A, B** shows examples of comparable fissures at the foot of the marginal scarps of collapse sinkholes developed on well-bedded sub-horizontal evaporites deposited in a playa-lake environment in the Ebro Cenozoic Basin, NE Spain (Gutiérrez et al., 2005).
- The inventoried depressions of Kotido crater display morphologic and morphometric characteristics comparable to those reported for other enclosed depressions on Mars attributed to dissolution, such as Tithonium Chasma (Baioni and Wezel, 2010; Baioni and Sgavetti, 2013), Coprates Chasma (Baioni et al., 2011), Hebes Chasma (Grindrod and Balme, 2010), Sinus Meridiani (Baioni and Sgavetti, 2013; Flahaut et al., 2015), Iani Chaos (Baioni and Tramontana, 2015), Tyrrhena Terra (Baioni and Tramontana, 2016), Western Noctis Labyrinthus (Baioni, 2018), and other regions (McKey and Nedell, 1988; Schaeffer, 1990; Spencer and Fanale, 1990).
- Some morphometric parameters of the depressions, such as the major axis (8-342 m), the area (44-29,371 m²), the volume (average 3,149 m³), and the depth (average 2.8 m),

are comparable with the broad range of values documented for sinkholes on Earth. A summary table with morphometric data can be found in Baioni (2018) although these metrics have a limited diagnostic meaning. Nonetheless, the large number of depressions mapped in Kotido crater offers the opportunity to generate statistically significant frequency-size relationships and comparing them with those produced with datasets of karst sinkholes from different karst settings on Earth (i.e., evaporites and carbonates, mantled and interstratal karst, epigene and hypogene karst). In the case of Kotido crater, the best fit between different size parameters (major axis, area, and volume) and their cumulative frequency is obtained with logarithmic functions ($R^2 \geq 0.94$) (**Fig. 5**). Similarly, regressions generated with the major axis of sinkholes on Earth developed in: (1) a limestone karst mantled by a thin alluvial cover (Val d'Orleans, France; Gombert et al., 2015); (2) a limestone karst mantled by a thick cohesive cover (Hamedan plains, Iran; Taheri et al., 2015); (3) a salt karst with a residual caprock (Gotvand salt pillow, Iran; Gutiérrez and Lizaga, 2016); (4) an epigene evaporite karst with both caprocks and covers (Fluvia valley, NE Spain; Gutiérrez et al., 2016); and (5) a hypogene interstratal evaporite karst (Sant Miquel valley, NE Spain; Gutiérrez et al., 2019), also show a high correlation ($R^2 \geq 0.92$) between the empirical data and logarithmic functions (**Fig. 8**). The variable slopes and size distributions of those datasets from different settings are attributed to factors such as the nature, thickness and mechanical strength of the cavity-roof materials (Gutiérrez et al., 2019). Corral and González (2018), using large datasets of karst depressions from the limestone karsts of Kentucky and Florida, and the mantled salt karst of the Dead Sea, obtained better fits with log-normal distributions. However, most of the depressions from Florida and Kentucky are not subsidence sinkholes, but solution sinkholes, and a great part of the depressions inventoried in the Dead Sea are uvalas (i.e., compound sinkholes). In Kotido crater and in the different areas on Earth indicated above, there is typically a deviation between the empirical data and the regressions for extreme-size values. The upper tail (small-size values), with lower empirical frequencies, is generally attributed to the incompleteness of the inventories and to mechanical thresholds. The first factor, typically related to lack of resolution of the remote-sensed data, presence of vegetation and human activity (e.g., anthropogenic filling), does not seem to be applicable to Kotido crater. The lower tail (large-size values), with higher observed frequencies, can be attributed to the coalescence of depressions (e.g., Corral and González, 2018; Gutiérrez et al., 2019). The process of coalescence involves a reduction in the number of depressions and an abrupt increase in the size of some depressions,

which may plot as outliers. Overall, the depressions of Kotido crater show larger dimensions than those mapped in epigene evaporite karst terrains on Earth, showing a striking parallelism with those of the Gotvand salt karst of Iran (**Fig. 8**). Potential collapse sinkholes on Mars should attain larger dimensions than on Earth under equivalent geometrical and mechanical conditions, given the lower gravitational acceleration (3.7 ms^{-2} versus 9.8 ms^{-2}) (Smith et al., 2006). For instance, a cylindrical cavity roof (i.e., flat ceiling) on Mars should have a diameter 1.6 times larger than that on Earth with the same weight. Moreover, as explained below, the depressions of Kotido crater seem to have been significantly reshaped and enlarged by long-sustained erosion.

- The orientation of the major axis of the elongated depressions show a broad prevalent N20-80E trend. This range covers the dominant orientation of the 1341 mapped features (N10-50) and the wind direction inferred from the 250 mapped dune fields (N60-80E) (**Fig. 4**). The depressions tend to occur spatially associated with fractures (**Fig. 3B, C**) and the highest density of depressions concurs with the zone showing the highest density of fractures (**Fig. 6**). These data support that the fracture system has played a significant role on the development and distribution of the depressions. In karst systems, fractures are major elements controlling the formation of subsurface cavities and the associated collapse sinkholes. These discontinuities provide preferential pathways for groundwater flow, which enlarge by dissolution through a self-accelerating process (e.g., Dreybrodt and Grabovsek, 2004; Ford and Williams, 2007; Palmer, 2009). They also contribute to reduce the rock-mass strength, favouring the collapse of cavity roofs. For instance, Dogan and Ozel (2005) found a good correlation between the distribution and orientation of collapse sinkholes in the epigene gypsum karst of Sivas, Turkey, and the fracture system. Another striking example is given by the high density of collapse sinkholes (ring of cenotes) associated with the margin of the Chicxulub impact crater in Yucatán, related to the higher degree of fracturing in the carbonate bedrock (Perry et al., 1995).

- Two main karst systems can be differentiated from the speleogenetic perspective: epigene and hypogene (Palmer, 2007; Klimchouk, 2007; Gutiérrez et al., 2019). Epigene systems are characterised by a dominant downward groundwater flow from recharge areas towards a topographically lower discharge zone, controlled by the base level of erosion and the associated water table. In hypogene systems karstification is caused by rising groundwater flows coming from an underlying aquifer, typically under confined

conditions (artesian aquifer). According to Pondrelli et al. (2019), the ELDs of Kotido crater were deposited in a playa-lake environment fed by artesian groundwater flows. Significant karstification during this stage was unlikely, since the groundwater was presumably highly mineralized leading to the precipitation of evaporites. However, the layered deposits in which the depressions have been formed are perched around 120 m above the deepest point of the crater. These are adequate topographic conditions for the development of an epigene karst system in the study area, which could be affected by downward groundwater flows towards a topographic base level. In epigene systems karst is generally expressed through widely distributed features such as caves and sinkholes, whereas in hypogene environments those features tend to form dense clusters separated by regions of minimal karst development (Klimchouk, 2003; Frumkin and Fischhendler, 2005; Gutiérrez et al., 2019). The NNI of 0.82 calculated for the depressions of study area, which indicates overall limited clustering of the depressions, is consistent with an epigene environment characterised by karst landforms distributed over the entire investigated zone (**Fig. 2**).

The depressions display a number of features and spatial relationships strongly suggesting that they have been re-shaped and enlarged by aeolian erosion, probably under the current wind regime. The rose diagram constructed with the wind directions inferred from the dune fields show a prevalent one-directional N60-80 trend (sense of flow), coherent with the NE-oriented yardangs documented in the area (Pondrelli et al., 2019) and the dominant azimuth of the major axes of the depressions (N20-80E) (**Fig. 4**). Numerous depressions show a markedly asymmetric morphology, with more subdued and irregular edges on the downwind NE edge, where the wind has a higher erosional capability due to flow concentration and higher vorticity (Whitney, 1978) (**Fig. 3A, B, C**). Moreover, some depressions show a stepped floor with smaller nested depressions typically associated with the SW sector (**Fig. 3D**). This type of geomorphic arrangement with nested surfaces is frequently observed in the floor of pans generated by aeolian deflation (e.g., Goudie and Wells, 1995). **Figure 7C, D** illustrates a comparable situation in the central sector of the Ebro Cenozoic Basin, NE Spain, where sinkholes related to gypsum dissolution show a very irregular downwind edge related to wind erosion and the development of yardangs (Gutiérrez-Elorza et al., 2002). These basins that may host saline ephemeral lakes also show nested depressions associated the upwind sector that record deepening phases attributed to periods with more intense aeolian action (Gutiérrez et al., 2013).

Other hypotheses could be proposed to explain the origin of the closed depressions mapped in Kotido crater. However, the available data tend to either refute them or strongly question their potential validity: (1) Wind erosion: although wind erosion may have played a significant role in the morphological evolution and expansion of the depressions as explained above, it cannot explain the ground deformation features associated with the rims of the depressions, which are indicative of brittle collapse. Moreover, blowout hollows develop by differential deflation on loose dune deposits (Hesp, 2002; Kuznetsov et al., 2005), whereas the analysed depressions formed on over-consolidated layered sediments. (2) Impact craters: these features can be ruled out by the non-circular geometry of the depressions (e.g., Barlow and Bradley, 1990; De Pablo and Komatsu, 2009), with an average elongation ratio of 0.7 (**Table 2**), and the lack of raised rims and ejecta. Impact craters in which the rims have been removed by backwearing are characterised by parabolic or super-parabolic cross-sections (Forsberg-Taylor et al., 2004; Watters et al., 2015), and the crater walls show a progressive slope decrease towards the bottom of the depression (Craddock et al., 2008). These morphological features are not observed in the depressions of Kotido crater, characterised by flat or stepped floors and steep walls. (3) Volcanic processes: depressions related to volcanic activity and products such as calderas, explosion craters or sinkholes related to the collapse of lava tubes can be confidently ruled out due to the lack of volcanic materials and landforms, the size of the depressions, and their spatial patterns (e.g., Palmer, 2009; Soare et al., 2013; Gutiérrez and Gutiérrez, 2016). (4) Hydrothermal processes: depressions related to the upwelling of groundwater can be ruled out by the aggregate volume of the depressions (ca. 1.610^6 m^3), their elongated shape and the lack of features such as vents, rimstones or outflow channels (e.g., Pellicer et al., 2014). (5) Thermokarst: subsidence related to the loss of ground ice by sublimation typically produces depressions with a desiccated regolith in their floor riddled by pockmarks and pits (Soare et al., 2008; Dundas et al., 2015). Moreover, these depressions are typically associated with patterned ground, as documented in the Utopia and western Elysium Planitia, and Astepus Colles regions (Soare and Osinski, 2009). Such landforms are considered to be diagnostic of periglacial activity (Soare et al., 2012).

The closed depressions mapped in the evaporite-bearing ELDs of Kotido crater are likely related to past subsurface dissolution by liquid water and the subsidence of the overlying

sediments. The resulting collapse depressions seem to have been reshaped by aeolian erosion, acting more intensively on their NE side, and rock-falls from the scarped margins, both causing enlargement of the depressions and eventually leading to their coalescence. The liquid water responsible for the dissolution may have been derived from the melting of snow and/or ice, including permafrost, as it has been proposed to explain the karst-like landforms found in other regions of Mars (Baioni et al., 2009; Grindrod and Balme, 2010; Jackson et al., 2011; Baioni and Sgavetti, 2013; Flahaut et al., 2015; Baioni and Tramontana, 2016; Baioni, 2018).

Episodic changes in Martian obliquity may explain the origin of the ice and/or snow that melted and generated these putative karst landforms in this equatorial region (Mustard et al., 2001; Laskar et al., 2004). Theoretical considerations about the stability of water ice and numerical climatic simulations predict that accumulation areas of ice and/or snow at the surface may have shifted repeatedly between polar, middle, tropical and equatorial latitudes in response to changes in the Martian axial tilt and atmospheric characteristics in the past (Forget et al., 2006; Madeleine et al., 2009; Wordsworth et al., 2013). According to some simulations, the net ice accumulation rates might have exceeded 20 mm/yr in locations around the Martian equator. Such shifts may have been necessary to achieve the Amazonian environmental conditions, given the current composition of the atmosphere (Madeleine et al., 2009), and other physical conditions (e.g., insolation, atmospheric circulation) in the past (Wordsworth et al., 2013). Moreover, recent retrospective studies have hypothesised the presence of ice in the tropical regions, as well as the presence of ground ice in equatorial zones (Shean, 2010; Mège and Bourgeois, 2011; Gourronc et al., 2014).

Some studies illustrate that impact craters and troughs may function as preferential areas for the accumulation of ice. Their interior behave as cold traps that tend to shield volatile elements from ablative insolation and wind circulation, favouring the preservation of icy bodies that would not persist in open plains. In the craters snow or ice accumulation presumably resulted from concentrated synoptic precipitation (Shean, 2010; Weitz et al., 2013), which may have resulted into significant runoff upon melting (Shean, 2010; Grant and Wilson, 2012; Weitz et al., 2013). In fact, in equatorial regions, the melting of rapidly emplaced and localized snow with the albedo of dust is possible for a subset of orbital conditions, even with the weak present-day greenhouse effect (Kite et al., 2011).

Moreover, recent works reveal the possibility of the presence of liquid water on the Martian surface in many regions even during the Amazonian epoch (Chapman et al., 2010; Morgan et al., 2011; Soare et al., 2013; Johnsson et al., 2014; de Haas et al., 2015; Salese et al., 2016; Frances et al., 2017; Hargitai and Gulick, 2018).

Regarding the chronology of the depressions, cartographic and geomorphic relationships indicate that they were formed after the deposition of the ELDs, with a poorly constrained early Hesperian age (Pondrelli et al., 2015), and most probably after the erosional phase within Kotido crater that placed the ELDs in a perched position with respect to the deepest zone of the crater. The absence of impact craters supports a young age for the depressions. Moreover, the presence of open marginal fissures suggests recent subsidence activity. It should be taken into account that the depressions are interpreted to be related to two processes that do not necessarily operate concomitantly: subsurface dissolution and collapse (Gutiérrez, 2016). In many regions on Earth, a significant time lag has been documented between the karstification periods and the timing of sinkhole development (e.g., Youssef et al., 2015). The formation of sinkholes may be related to the collapse of cavities formed long time before. Most probably, the subsurface dissolution responsible for the development of the depressions in Kotido crater occurred sometime in the past under climatic conditions different from the present day, and the fissures may be the manifestation of residual subsidence activity related to the presence of relict cavities. The geomorphic appearance of the depressions of Kotido crater (e.g., degradation of margins, infill) suggests a similar or younger age to those observed in other region of Mars ascribed to the early Amazonian (Baioni and Wezel, 2010; Baioni et al., 2011; Baioni and Tramontana, 2016), and appear to be older than others of late Amazonian age (Baioni and Tramontana, 2015; Baioni, 2018).

6. Conclusions

The analysed closed depressions, which developed in the ELDs within Kotido crater are likely related to subsurface dissolution of evaporites and collapse processes (i.e., collapse sinkholes). The development of underground voids and the collapse of cavity roofs is supported by the presence of open fissures at the foot of the scarped margins of some depressions. The dimensions of the depressions, including compound basins related to coalescence, are comparable with those reported for sinkholes on Earth and Mars. Moreover, the cumulative frequency of the major axis of the depressions in Kotido crater

follow a logarithmic distribution, like in numerous evaporite and carbonate karst regions of Earth. The apparently larger size of the depressions of Kotido crater, compared with other epigene evaporite karst areas on Earth may be related to the lower gravitational acceleration of Mars. The spatial association between depressions and fractures, and the preferred orientation of the elongated depressions (N20-80E) and the fractures (N10-50E), suggest that both dissolution and subsidence processes were influenced by these permeability and mechanical-weakness features. The topographic conditions, with the area perched more than 100 m above the deepest zone of the crater, and the overall random distribution of the inventoried depressions (NNI: 0.82), are consistent with an epigene karst in which dissolution was caused by downward groundwater flows. The putative karst depressions seem to have been enlarged and reshaped by long-sustained wind erosion. This is supported by (1) the trend of the one-directional winds (N60-80E) inferred from dune fields, coherent with the orientation of the elongated depressions (N20-80E); (2) the presence of NE-oriented yardangs; and (3) the frequent asymmetry of the depressions, with a more irregular and degraded NE margin and nested depressions associated to the upwind side.

The investigated depressions are most probably relict landforms related to dissolution of evaporites in the past. These may be indicative markers of past paleoclimatic and paleohydrological conditions during which there was significant underground circulation of liquid water, presumably derived from the melting of snow and/or ice. The fissures observed at the margins of some depressions are consistent with residual subsidence activity related to the presence of subsurface cavities formed in the past. The relatively fresh appearance of the depressions, the lack of impact craters, and the comparison with depressions documented in other regions suggest a loosely constrained Amazonian age.

Acknowledgements

This work has been supported by project CGL2017-85045-P (Ministerio de Ciencia, Innovación y Universidades, Gobierno de España).

References

Andrews-Hanna J. C., Zuber M. T., Arvidson R. E., Wiseman S. M., 2010. Early Mars hydrology: Meridiani playa deposits and the sedimentary record of Arabia Terra. *Journal of Geophysical Research: Planets*, 115 (E6). doi: 10.1029/2009JE003485.

Baioni D., Zupan Hajna N., Wezel F.C., 2009. Karst landforms in a Martian evaporitic dome. *Acta Carsologica*, 38(1), 9-18. Retrieved from <https://search.proquest.com/docview/869787639?accountid=14795>.

Baioni D., Wezel F. C., 2010. Morphology and origin of an evaporitic dome in Tithonium Chasma, Mars. *Planetary and Space Science* 58, 847-857. doi: 10.1016/j.pss.2010.01.009.

Baioni D., Zupan Hajna N., Wezel F. C., 2011. Karst landforms in an interior layered deposit within Coprates chasma, Mars. *Acta Carsologica* 40(3), 473-481. Retrieved from <https://search.proquest.com/docview/1668230512?accountid=14795>.

Baioni D., 2013. Morphology and geology of an interior layered deposit in the western Tithonium Chasma, Mars. *Planetary and Space Science* 89, 140-150.

Baioni D., Sgavetti M., 2013. Karst terrains as possible lithologic and stratigraphic markers in northern Sinus Meridiani, Mars. *Planetary and Space Science* 75(1), 173-181. doi: 10.1016/j.pss.2012.08.011.

Baioni D., Tramontana M., 2015. Evaporite karst in three interior layered deposits in Iani Chaos, Mars. *Geomorphology* 245, 15-22. doi: 10.1016/j.geomorph.2015.05.018.

Baioni D., Tramontana M., 2016. Possible karst landforms in two unnamed craters in Tyrrhena Terra, Mars. *Planetary and Space Science* 132, 57-65. doi: 10.1016/j.pss.2016.08.011.

Baioni D., Tramontana M., 2017. "Possible evaporite karst in an interior layered deposit in Juventae Chasma, Mars. *International Journal of Speleology* 46, 181-189.

Baioni D., 2018. Karst landforms as markers of recent climate change on Mars: an example from a Late Amazonian Epoch evaporate-karst within a trough in western Noctis Labyrinthus. *Dynamic Mars: Recent and Current Landscape Evolution of the Red Planet*. Elsevier, Amsterdam, Netherlands, 411-429. doi: 10.1016/B978-0-12-813018-6.00014-5.

Baioni D., 2019. Very recent karst landforms within Cagli crater, Sinus Meridiani, Mars. *Italian Journal of Geosciences* 138, 262-273.

Barlow N. G., Bradley T. L., 1990. Martian impact craters: Dependence of ejecta and interior morphologies on diameter, latitude, and terrain. *Icarus*, 87, 156-179. doi: doi.org/10.1016/0019-1035(90)90026-6.

Beyer, R. A., Alexandrov, O., McMichael, S., 2018. The Ames Stereo Pipeline: NASA's open source software for deriving and processing terrain data. *Earth and Space Science*, 5(9), 537-548.

Bibring J. P., Langevin Y., Mustard J. F., Poulet F., Arvidson R., Gendrin A., Gondet B., Mangold N., Pinet P., Forget F., the OMEGA team, 2006. Global mineralogical and aqueous Mars history derived from OMEGA/Mars express data. *Science* 312(5772), 400-404. doi: 10.1126/science.1122659.

Carr M. H., 2012. The fluvial history of Mars. *Philosophical Transactions of the Royal Society A: Mathematical, Physical and Engineering Sciences*, 370(1966), 2193-2215. doi: 10.1098/rsta.2011.0500.

Chapman M. G., Neukum G., Dumke A., Michae G., van Gasselt S., Kneissl T., Zuschneid W., Hauber E., Mangold N., 2010. Amazonian geologic history of the Echus Chasma and Kasei Valles system on Mars: New data and interpretations. *Earth and Planetary Science Letters* 294(3-4), 238–255. doi: 10.1016/j.epsl.2009.11.034.

Clark P. J., Evans F. C., 1954. Distance to nearest neighbor as a measure of spatial relationships in populations. *Ecology*, 35(4), 445-453. doi: 10.2307/1931034.

Corral, Á., González, Á. , 2019. Power-law size distributions in geoscience revisited. *Earth and Space Science*, 6. doi: 10.1029/2018EA000479.

Craddock, R. A., Ansan, V., Howard, A. D., Mangold, N., 2008. Crater modification processes in the aeolis region of Mars. In: *Lunar and Planetary Science Conference Abstracts*, vol. 39. The Woodlands, Texas, p. #1617.

De Pablo M. A., Komatsu G., 2009. Possible pingo fields in the Utopia basin, Mars: Geological and climatical implications. *Icarus*, 199(1), 49-74. doi: 10.1016/j.icarus.2008.09.007.

Croft, S.K., 1989. Spelunking on Mars: The carbonate-tectonic hypothesis for the origin of Valles Marineris. In: Watters, T.R., Golombek, M.P. (Eds.). MEVTV Workshop on Tectonic Features on Mars. Lunar and Planetary Institute Report 89-06, 21-24.

De Carvalho-Junior O. A., Fontes-Guimaraes R., Montgomery D. R., Gillispie A. R., Trancoso-Gomes R. A., de Souza-Martins E., Correia-Silva N., 2014. Karst depression detection using ASTER, ALOS/PRISM and SRTM-derived digital elevation models in the Bambuí Group, Brazil. *Remote Sensing*, 6, 330-351. doi: 10.3390/rs6010330.

De Haas T., Hauber E., Conway s.j., van Steijn H., Johnsson A., Kleinhans M. G., 2015. Earth-like aqueous debris-flow activity on Mars at high orbital obliquity in the last million years. *Nature Communication*, 6, 7543. doi: 10.1038/ncomms8543.

Doctor D. H., Young J. A., 2013. An evaluation of automated GIS tools for delineating karst sinkholes and closed depressions from 1-meter LIDAR-derived digital elevation data. In L. Land, D.H. Doctor, & J.B. Stephenson (Eds.), *Sinkholes and the engineering and environmental impacts of karst* (pp. 449-458). Carlsbad: National Cave and Karst Research Institute. doi: 10.5038/9780979542275.1156.

Dogan U., Ozel S., 2005. Gypsum karst and its evolution east of Hafik (Sivas, Turkey). *Geomorphology* 71(3-4), 373-388. doi: 10.1016/j.geomorph.2005.04.009.

Dreybrodt W., Gabrovsek F., 2004. Speleogenesis: computer models. In: Gunn, J. (Ed.). *Encyclopedia of Caves and Karst Science*. Fitzroy Dearborn, 677-681.

Dundas C. M., Byrne S., McEeven A. S., 2015. Modelling the development of Martian sublimation thermokarst landforms. *Icarus*, 262, 154-169. doi: 10.1016/j.icarus.2015.07.033.

Ferguson R. L., Hare T. M., Laura J., 2018. HRSC and MOLA Blended Digital Elevation Model at 200m v2, Astrogeology PDS Annex, U.S. Geological Survey. URL: http://bit.ly/HRSC_MOLA_Blend_v0.

Flahaut J., Carter J., Poulet F., Bibring J.P., van Westrenen W., Davies G.R., Murchie S. L., 2015. Embedded clays and sulfates in Meridiani Planum, Mars. *Icarus* 248, 269-288. doi: 10.1016/j.icarus.2014.10.046.

Ford D., Williams P., 2007. *Karst Hydrogeology and Geomorphology*. Wiley, 562.

Forget F., Haberle R. M., Montmessin F., Levrard B., Head J. W., 2006. Formation of glaciers on Mars by atmospheric precipitation at high obliquity. *Science*, 311(5759), 368–371. doi: 10.1126/science.1120335.

Forsberg-Taylor N. K., Howard A. D., Craddock R. A., 2004. Crater degradation in the Martian highlands: Morphometric analysis of the Sinus Sabaeus region and simulation modeling suggest fluvial processes. *Journal of Geophysical Research: Planets*, 109(E5),. doi: 10.1029/2004JE002242.

Frances E. G., Butcher G., Balme M. R., Gallagher C., Arnold S. J., Conway S. J., Hagermann A., Lewis S. R., 2017. Recent Basal Melting of a Mid-Latitude Glacier on Mars. *Journal of Geophysical Research: Planets*, 122(12), 2445-2468. doi: 10.1002/2017JE005434.

Franchi F., Rossi A., Pondrelli M., Cavalazzi B., 2014. Geometry, stratigraphy and evidences for fluid expulsion within Crommelin crater deposits, Arabia Terra, Mars. *Planetary and Space Science*, 92, 34-48. doi: 10.1016/j.pss.2013.12.013.

Frumkin, A., Fischhendler, I., 2005. Morphometry and distribution of isolated caves as a guide for phreatic and confined paleohydrological conditions. *Geomorphology*, 67, 457–451.

García-Arnay, Á., Gutiérrez, F., Fernández, S., 2018. Coastal-Like Features in *Nepenthes Mensae*, Mars as Paleowater-Level Indicators, and a Terrestrial Analog. In: Lunar and Planetary Science Conference Abstracts, vol. 49. The Woodlands, Texas, p#2595.

Garvin J. B., Sakimoto S., and Frawley J. J., 2003. Craters on Mars: Global geometric properties from gridded MOLA topography. In: Sixth International Conference on Mars, Abstract #3277.

Gendrin A., Mangold N., Bibring J. P., Langevin Y., Gondet B., Poulet F., Bonello G., Quantin C, Mustard J. and Arvidson R., 2005. Sulfates in martian layered terrains: The OMEGA/Mars Express view. *Science*, 307(5715), 1587-1591. doi: 10.1126/science.1109087.

Gombert, P., Orsat, J., Mathon, D., Alboresha, R., Al Heib, M., Deck, O., 2015. Role des effondrements karstiques sur les désordres survenus sur les digues de Loire dans le Val D'Orleans (France). *Bulletin of Engineering Geology and Environment* 74(1), 125–140. doi: 10.1007/s10064-014-0594-8.

Goudie A. S., Wells G. L., 1995. The nature, distribution and formation of pans in arid zones. *Earth-Science Reviews* 38(1), 1-69. doi: 10.1016/0012-8252(94)00066-6.

Gourronc M., Bourgeois O., Megè D., Pochat S., Bultei B., Massè M., Le Deil L., Le Mouèlic S., Mercier D., 2014. One million cubic kilometers of fossil ice in Valles Marineris: Relicts of a 3.5 Gy old glacial landsystem along the Martian equator. *Geomorphology*, 204, 235-255. doi: 10.1016/j.geomorph.2013.08.009.

Grant J. A., Wilson S. A., 2012. A possible synoptic source of water for alluvial fan formation in southern Margaritifer Terra, Mars. *Planetary and Space Science*, 72(1), 44-52. doi: 10.1016/j.pss.2012.05.020.

Grindrod P. M., Balme M. R., 2010. Groundwater processes in Hebes Chasma, Mars. *Geophysical Research Letters* 37(13), L13202. doi: 10.1029/2010GL044122, 2010.

Gutiérrez-Elorza M., Desir G., Gutiérrez-Santolalla F., 2002. Yardangs in the semiarid central sector of the Ebro Depression (NE Spain). *Geomorphology* 44(1-2), 155-170. doi: 10.1016/S0169-555X(01)00151-9.

Gutiérrez, F., 2016. Sinkhole hazards. *Oxford Research Encyclopedia of Natural Hazard Science*. Oxford University Press, 1-92.

Gutiérrez F., Gutiérrez-Elorza M., Marín C., Desir G., Maldonado C., 2005. Spatial distribution, morphometry and activity of La Puebla de Alfindén sinkhole field in the Ebro river valley (NE Spain): Applied aspects for hazard zonation. *Environmental Geology* 48(3), 360-369. doi: 10.1007/s00254-005-1280-8.

Gutiérrez F., Johnson K., Cooper A., 2008. Evaporite karst processes, landforms, and environmental problems. *Environmental Geology* 53(5), 935-936. doi: 10.1007/s00254-007-0715-9.

Gutiérrez F., Cooper A., 2013. Surface Morphology of Gypsum Karst. *Treatise on Geomorphology, Karst Geomorphology*, Vol. 6, 425-437. doi: 10.1016/B978-0-12-374739-6.00114-7.

Gutiérrez F., Valero-Garcés B., Desir, G., González-Sampériz P., Gutiérrez M., Linares R., Zarroca M., Moreno A., Guerrero J., Roqué C., Arnold L.J., Demuro M., 2013. Late Holocene evolution of playa lakes in the central sector of the Ebro Depression based on geophysical surveys and morpho-stratigraphic analysis of lacustrine terraces. *Geomorphology*, 196, 177-197. doi: 10.1016/j.geomorph.2012.02.013.

Gutiérrez F., Parise M., De Waele J., Jourde H., 2014. A review on natural and human-induced geohazards and impacts in karst. *Earth-Science Reviews* 138, 61-88. doi: 10.1016/j.earscirev.2014.08.002.

Gutiérrez F., Gutiérrez M., 2016. *Landforms of the Earth. An illustrated guide*. Springer, 270. doi: 10.1007/978-3-319-26947-4.

Gutiérrez, F., Fabregat, I., Roqué, C., Carbonel, D., Guerrero, J., García-Hermoso, F., Zarroca, M., Linares, M., 2016. Sinkholes and caves related to evaporite dissolution in a stratigraphically and structurally complex setting, Fluvia Valley, eastern Spanish Pyrenees. Geological, geomorphological and environmental implications. *Geomorphology* 267, 76–97. doi: 10.1016/j.geomorph.2016.05.018.

Gutiérrez, F., Lizaga, I., 2016. Sinkholes, collapse structures and large landslides in an active salt dome submerged by a reservoir: the unique case of the Ambal ridge in the Karun River, Zagros Mountains, Iran. *Geomorphology* 254, 88–103. doi: 10.1016/j.geomorph.2015.11.020.

Gutiérrez F., Fabregat I., Roqué C., Carbonel D., Zarroca M., Linares R., Yechieli Y., García-Arnay Á., Sevil J., 2019. Sinkholes in hypogene versus epigene karst systems, illustrated with the hypogene gypsum karst of the Sant Miquel de Campmajor Valley, NE Spain. *Geomorphology* 328: 57-78. doi: 10.1016/j.geomorph.2018.12.003.

Hargitai H. I., Gulick V.C., 2018. Late Amazonian–Aged Channel and Island Systems Located East of Olympus Mons, Mars. In: *Dynamic Mars: Recent and Current Landscape Evolution of the Red Planet*. Elsevier, Amsterdam, Netherlands, pp. 121-154. doi: 10.1016/B978-0-12-813018-6.00004-2.

Hesp P., 2002. Foredunes and blowouts: initiation, geomorphology and dynamics. *Geomorphology*, 48(1-3), 245-268. doi: 10.1016/S0169-555X(02)00184-8.

Hynek B. M., Di Achille G., 2017. Geologic map of Meridiani Planum, Mars. US Geological Survey Scientific Investigations Map, 3356.

Jackson M. P. A., Adams J. B., Dooley A. R., Montgomery D. R., 2011. Modelling the collapse of Hebes Chasma, Valles Marineris, Mars. *Geological Society of America Bulletin* 123(7-8), 1596-1627. doi: 10.1130/B30307.1.

Johnson K. S., 2008. Evaporite-karst problems and studies in the USA. *Environmental Geology* 53(5), 937-943. doi: 10.1007/s00254-007-0716-8.

Johnsson A., Reiss D., Hauber E., Hiesinger H., Zanetti M., 2014. Evidence for very recent melt-water and debris flow activity in gullies in a young mid-latitude crater on Mars. *Icarus*, 235, 37-54. doi:10.1016/j.icarus.2014.03.005.

Kite E. S., Michaels T. I., Rafkin S., Manga M., Dietrich W. E., 2011. Localized precipitation and runoff on Mars. *Journal of Geophysical Research: Planets*, 116(E7). doi: 10.1029/2010JE003783.

Klimchouk A. B., 2003. Conceptualization of speleogenesis in multi-story artesian systems: a model of transverse speleogenesis. *Speleogenesis and Evolution of Karst Aquifers* 1, 1–18.

Klimchouk A. B., 2007. Hypogene speleogenesis: hydrogeological and morphogenetic perspective. National Cave and Karst Research Institute. Special paper 1, 106.

Kuznetsov I. V., Kuzmin R. O., Greeley R., 2005. Wind-related erosion depressions within a small impact craters in Chryse and Elysium Planitia, Mars. In: *Lunar and Planetary Science Conference Abstracts*, vol. 36. The Woodlands, Texas, p#1810.

Laskar J., Correia A. C. M., Gastineau M., Joutel F., Levrard B., Robutel P., 2004. Long term evolution and chaotic diffusion of the insolation quantities of Mars. *Icarus* 170(2), 343–364. doi: 10.1016/j.icarus.2004.04.005.

Luzzi E., Rossi A. P., Pozzobon R., Oehler D. Z., Etioppe G., 2018. Becquerel Crater Radial Faults: A Possible Target for Methane Seepage Investigations. In: *Lunar and Planetary Science Conference*, Vol. 49.

Madeleine J. B., Forget F., Head J. W., Levrard B., Montmessin F., Millaur E., 2009. Amazonian northern mid-latitude glaciation on Mars: A proposed climate scenario. *Icarus*, 203(2), 390-405. doi: 10.1016/j.icarus.2009.04.037.

Malin M. C., Edgett K. S., 2000. Sedimentary Rocks of Early Mars. *Science*, 290(5498), 1927-1937. doi: 10.1126/science.290.5498.1927.

Mangold N., Gendrin A., Gondet B., LeMouelic S., Quantin C., Ansan V., Bibring J. P., Langevin Y., Masson P., Neukum G., 2008. Spectral and geological study of the sulfate-rich region of West Candor Chasma, Mars. *Icarus*, 194(2), 519–543. doi: 10.1016/j.icarus.2007.10.021.

McEwen A. S., Eliason E. M., Bergstrom J. W., Bridges N. T., Hansen C. J., Delamere W. A., Grant J. A., Gulick V. C., Herkenhoff K. E., Keszthelyi L., Kirk R. L., Mellon M. T., Squyres S. W., Thomas N., Weitz C. M., 2007. Mars reconnaissance orbiter's high-resolution imaging science experiment (HiRISE). *Journal of Geophysical Research: Planets*, 112(E5). doi: 10.1029/2005JE002605.

McKay C. P., Nedell S. S., 1988. Are there carbonate deposits in Valles Marineris, Mars? *Icarus*, 73(1), 142–148. doi: 10.1016/0019-1035(88)90088-7.

Mège D., Bourgeois O., 2011. Equatorial glaciations on Mars revealed by gravitational collapse of Valles Marineris wall slope. *Earth and Planetary Science Letters*, 310(3-4), 182-191. doi: 10.1016/j.epsl.2011.08.030.

Miller V. C., 1953. A quantitative geomorphic study of drainage basin characteristics in the Clinch Mountain area. Technical report 3, Department of Geology, Columbia University.

Morgan G. A., Head J. W., Marchant D. R., 2011. Preservation of Late Amazonian Mars ice and water-related deposits in a unique crater environment in Noachis Terra: Age relationships between lobate debris tongues and gullies. *Icarus*, 211(1), 347-365. doi: 10.1016/j.icarus.2010.08.004.

Murchie S., Arvidson R., Bedini P., Beisser K., Bibring J. P., Bishop J., Boldt J., Cavender P., Choo T., Clancy R. T., Darlington E. H., Des Marais D., Espiritu R., Fort D., Green R., Guinness E., Hayes J., Hash C., Heffernan K., Hemmler J., Heyler G., Humm D., Hutcheson J., Izenberg N., Lee R., Lees J., Lohr D., Malaret E., Martin T., McGovern J. A., McGuire P., Morris R., Mustard J., Pelkey S., Rhodes E., Robinson M., Roush T., Schaefer E., Seagrave G., Seelos F., Silverglate P., Slavney S., Smith M., Shyong W. J., Strohbehn K., Taylor H., Thompson P., Tossman B., Wirzburger M., Wolff M., 2007. Compact reconnaissance imaging spectrometer for Mars (CRISM) on Mars

reconnaissance orbiter (MRO). *Journal of Geophysical Research: Planets*, 112(E5). doi: doi.org/10.1029/2006JE002682.

Mustard J. F., Cooper C. D., Rifkin M. K., 2001. Evidence for recent climate change on Mars from the identification of youthful near-surface ground ice. *Nature*, 412(6845), 411-414. doi: 10.1038/35086515.

Oehler D. Z., Allen C. C., 2008. Ancient hydrothermal springs in Arabia Terra, Mars. In: *Lunar and Planetary Science Conference Abstracts*, Vol. 39, p. #1391.

Okubo C. H., Schultz R. A., Chan M. A., Komatsu G., 2009. Deformation band clusters on Mars and implications for subsurface fluid flow. *Geological Society of America Bulletin*, 121(3-4), 474-482. doi: 10.1130/B26421.1.

Ori G., Baliva A., 1999. Large bulges at the center of impact craters on Mars. In: *Lunar and Planetary Science Conference Abstracts*, Vol. 30.

Palmer A. N., 2007. *Cave Geology*. Cave Books, Dayton, 454.

Pellicer X. M., Linares R., Gutiérrez F., Comas X., Roqué C., Carbonel D., Zarroca M., Rodríguez J. A. P., 2014. Morpho-stratigraphic characterization of a tufa mound complex in the Spanish Pyrenees using ground penetrating radar and trenching, implications for studies in Mars. *Earth and Planetary Science Letters*, 388, 197-210. doi: 10.1016/j.epsl.2013.11.052.

Perry E., Marin L., McClain J., Velázquez G., 1995. Rig of cenotes (sinkholes), northwest Yucatán, Mexico: Its hydrogeologic characteristics and possible association with the Chicxulub impact crater. *Geology* 23(1), 17-20. doi: 10.1130/0091-7613(1995)023<0017:ROCSNY>2.3.CO;2.

Pondrelli M., Baliva A., Di Lorenzo S., Marinangeli L., Rossi A. P., 2005. Complex evolution of paleolacustrine systems on Mars: An example from the Holden crater. *Journal of Geophysical Research: Planets*, 110(E4). doi: 10.1029/2004JE002335.

Pondrelli M., Rossi A. P., Ori G., van Gasselt S., Praeg D., Ceramicola S., 2011. Mud volcanoes in the geologic record of Mars: The case of Firsoff crater. *Earth and Planetary Science letters*, 304(3-4), 511-519. doi: 10.1016/j.epsl.2011.02.027.

Pondrelli, M., Rossi A. P., Le Deit L., Fueten F., van Gasselt S., Glamoclija M., Cavalazzi B., Hauber E., Franchi F., Pozzobon R., 2015. Equatorial layered deposits in Arabia Terra, Mars: Facies and process variability. *Geological Society of America Bulletin*, 127(7-8), 1064-1089. doi: 10.1130/B31225.1.

Pondrelli M., Rossi A. P., Le Deit L., Schmidt G. W., Pozzobon R., Hauber E. and Salese F., 2019. Groundwater control and process variability on the Equatorial Layered Deposits of Kotido crater, Mars. *Journal of Geophysical Research: Planets*, 124(E3), 779-800. doi: 10.1029/2018JE005656.

Preuschmann S., Benkkert D., Wagner R., Neukum, G., the HRSC Co-Investigator Team, 2006. Karst-like topography within the Ganges Chasma region. *Geophysical Research Abstract*, 8: 09383.

Robbins S., Hynek B., 2013. Utility of laser altimeter and stereoscopic terrain models: Application to Martian craters. *Planet Space Sci*, 86, 57–65. doi: 10.1016/j.pss.2013.06.019.

Rodriguez J.A.P., Zarroca M., Linares R., Gulick V., Weitz C.M., Yan J., Fairén A.G., Miyamoto H., Platz T., Baker V., Kargel J., Glines N., Higuchi K., 2016. Groundwater flow induced collapse and flooding in Noctic Labyrinthus, Mars. *Planetary and Space Science*, 124, 1-14. doi:10.1016/j.pss.2015.12.009

Rossi A., Neukum G., Pondrelli M., Gasselt S.V., Zegers T., Hauber E., Chicarro A., Foing B., 2008. Large-scale spring deposits on Mars? *Journal of Geophysical Research: Planets*, 113(E8). doi: 10.1029/2007JE003062.

Salese F., Di Achille, G., Neesemann A., Ori G. G., Hauber E., 2016. Hydrological and sedimentary analyses of well-preserved paleofluvial-paleolacustrine systems at Moa Valles, Mars. *Journal of Geophysical Research: Planets*, 121(2), 194-232. doi: 10.1002/2015JE004891.

Schaeffer M., 1990. Geochemical evolution of the northern plains of Mars: early hydrosphere, carbonate development and present morphology. *Journal of Geophysical Research: Solid Earth*, 95(B9), 14291-14300. doi: 10.1029/JB095iB09p14291.

Schon S. C., Head J. W., Fassett C. I., 2012. An overfilled lacustrine system and progradational delta in Jezero crater, Mars: Implications for Noachian climate. *Planetary and Space Science*, 67(1), 28-45. doi: 10.1016/j.pss.2012.02.003.

Schumm S. A., 1956. Evolution of drainage systems and slopes in badlands at Perth Amboy, New Jersey. *Geological Society of American Bulletin*, 67(5), 597-646. doi: 10.1130/0016-7606(1956)67[597:EODSAS]2.0.CO;2.

Shean D. E., 2010. Candidate ice-rich material within equatorial craters on Mars. *Geophysical Research Letters* 37(24), L24202. doi: 10.1029/2010GL045181.

Shean D. E., 2010. Candidate ice-rich material within equatorial craters on Mars. *Geophysical Research Letters* 37(24), L24202. doi: 10.1029/2010GL045181.

Smith, Z.E., Tullis, J.A., Steele, K.F., Malfavon, L., 2006. Martian sinkholes: Implications for large scale evaporite deposits. 37th Annual Lunar and Planetary Science Conference.

Soare R. J., Kargel J. S., Osinski G. R., Costard F., 2007. Thermokarst processes and the origin of crater-rim gullies in Utopia and western Elysium Planitia. *Icarus* 191(1), 95-112. doi: 10.1016/j.icarus.2007.04.018.

Soare R. J., Osinski G. R., 2009. Stratigraphical evidence of late Amazonian periglaciation and glaciation in the Astapus Colles region of Mars. *Icarus* 202(1), 17-21. doi: 10.1016/j.icarus.2009.02.009.

Soare R. J., Costard F., Pearce G. D., Sèjournè A., 2012. A re-interpretation of the recent stratigraphical history of Utopia Planitia, Mars: Implications for late-Amazonian periglacial and ice-rich terrain. *Planetary and Space Science* 60(1), 131-139. doi: 10.1016/j.pss.2011.07.007.

Soare R. L., Conway S. J., Pearce G. D., Dohm J. M., Grindrod P. M., 2013. Possible crater-based pingos, paleolakes and periglacial landscapes at the high latitudes of Utopia Planitia, Mars. *Icarus*, 225(2), 971-981. doi: 10.1016/j.icarus.2012.08.041.

Spencer J. R., Fanale P. F., 1990. New models for the origin of Valles Marineris closed depressions. *Journal of Geophysical Research*, 95(B9), 14301-14313. doi: 10.1029/JB095iB09p14301.

Taheri K., Gutiérrez F., Mohseni H., Raeisi E., Taheri M., 2015. Sinkhole susceptibility mapping using the analytical hierarchy process (AHP) and magnitude frequency relationship: a case study in Hamadan province, Iran. *Geomorphology* 234, 64–79. doi: 10.1016/j.geomorph.2015.01.005.

Tanaka K., Skinner J., Dohm J., Irwin R., Kolb E., Fortezzo C., Platz T., Michael G., Hare T., 2014. Geologic map of Mars. USGS Scientific Investigations Map 3292. doi: 10.3133/sim3292.

Watters W. A., Geiger L. M., Fendrock M., Gibson R., 2015. Morphometry of small recent impact craters on Mars: size and terrain dependence, short-term modification, *Journal of Geophysical Research: Planets*, 120(2), 226-254. doi: 10.1002/2014JE004630.

Watters, W. A., Geiger, L. M., Fendrock, M., Gibson, R., Hundal, C. B., 2017. The role of strength defects in shaping impact crater planforms. *Icarus*, 286, 15-34. doi: 10.1016/j.icarus.2016.12.024

Waltham A. C., 1989. Ground subsidence. Blackie, Glasgow and London, 202 p.

Weiz C. M., Bishop J. L., Grant J. A., 2013. Gypsum, opal and fluvial channels within a trough of Noctis Labyrinthus, Mars: Implications for aqueous activity during the late Hesperian to Amazonian. *Planetary and Space Science*, 87, 130-145. doi: 10.1016/j.pss.2013.08.007.

Whitney M. I., 1978. The role of vorticity in developing lineation by wind erosion. *Geological Society of America Bulletin*, 89(1), 1-18. doi: 10.1130/0016-7606(1978)89<1:TROVID>2.0.CO;2.

Williams M., 1972. Success and Failure in Analysis. Primary Envy and the Fate of the Good. *The journal of Analytical Psychology*, 17(1), 7-6.

Wordsworth R., Forget F., Millour E., Head J. W., Madeleine J. B., Charnay B., 2013. Global modelling of the early Martian climate under a denser CO₂ atmosphere: water cycle and ice evolution. *Icarus*, 222(1), 1–19. doi: 10.1016/j.icarus.2012.09.036.

Youssef A. M., Al-Harbi H. M., Gutiérrez F., Zabramwi Y. A., Bulkhi A. B., Zahrani S. A., Bahamil A. M., Zahrani A. J., Otaibi Z. A., El-Haddad B. A., 2016. Natural and human-induced sinkhole hazards in Saudi Arabia: distribution, investigation, causes and impacts. *Hydrogeology Journal* 24(3), 625-644. doi: 10.1007/s10040-015-1336-0.

Figure captions

Figure 1. General position of Kotido crater, Arabia Terra, in the equatorial region of Mars and location of the study area within the floor of Kotido crater, indicated in a DEM (~200 m/pixel) (left) (Fergason et al., 2018) and a CTX image mosaic from images F05_037663_1794 and B18_016776_1818 (right).

Figure 2. Geomorphological map of the study area showing the distribution of closed depressions and fractures, as well as the wind-direction vectors inferred from dune fields.

Figure 3. HiRISE images (ESP_016776_1810 and ESP_016921_1810) illustrating some of the main features of the study area and the mapped closed depressions. A: Elongated depressions with a broader and steeper SW side and a pointed and a gentler NE edge (stars). Sharp-crested NE-oriented ridge attributable to a yardang (arrow). B: Aligned and partially coalesced elongated depressions associated with fractures with a prevalent NNE trend. Note the difference between the gentler NE and steeper SW sides of the depressions and the prominent ridge-like morphology of some edges. C: Composite depressions with scarped edges developed on fractured light-toned resistant layers. The floor of the depressions is largely mantled by aeolian deposits a scattered fallen blocks. D: Elongated scarp-edged depressions some of them with stepped floors and nested basins associated with the SW sector. E and F: Depressions with fissures at the foot of the marginal scarps indicative of ground deformation. Butte capped by a resistant layer in the NE corner of the image. Inset images show enlarged fissures. Inset in figure F corresponds to a RGB image.

Figure 4. Rose diagrams showing the distribution of the orientation of the major axis of the depressions (A) and the fractures (B), and the wind directions inferred from fields of transverse dunes (C). (n: number of data).

Figure 5. Semi-log graphs of cumulative frequency (F_c) versus major axis (M_a), area (A), and volume (V) of the closed depressions, and best-fit regressions functions (dashed lines).

Figure 6. Kernel density models of depressions by area (A) and number (B) and of fractures (C).

Figure 7. Images of sinkholes developed on horizontally lying Tertiary evaporites in the Ebro Basin, NE Spain. A: Vertical view of collapse sinkholes with open fissures at the foot of the scarped margins (white arrows). The large sinkhole with tree vegetation is 85 m long and is centred at $41^{\circ}38.810'N$ $0^{\circ}45.501'W$. B: Field view of a scarped margin with an open fissure. C: Sinkhole developed on gypsum strata re-shaped by aeolian erosion. Note the irregular downwind edge with wind-fluted yardangs. Arrow indicates prevalent wind direction. The playa-lake in the foreground is centered at $41^{\circ}24.760'N$ $0^{\circ}9.086'W$. D: Shaded relief model of a sinkhole with digitated downwind edge and a nested depression associated with the upwind sector of the basin. Arrow indicates wind direction. Depression centred at $41^{\circ}24.183'N$ $0^{\circ}4.717'W$.

Figure 8. Frequency-size relationships constructed with the major axis of the depressions mapped in Kotido crater and sinkhole inventories from different karst regions of the Earth. See explanation in the text.

Parameter	Code	Definition	Procedure
Major axis	Ma	Straight line between most distant points of perimeter. Indicates elongation direction	Longest distance between two vertices of convex hull polygons generated with the depressions using the Minimum Bounding Geometry tool (Data Management Tools; Features)
Orientation of major axis	OMa	Azimuth of major axis	Attribute calculated automatically by the Minimum Bounding Geometry tool (Data Management Tools; Features)
Elongation ratio	Re	Ratio between the diameter of a circle with the same area as that of the depression and the major axis (Schumm, 1956)	$Re = D/Ma$ Virtual circle diameter given by $D = 2\sqrt{A/\pi}$
Area	A	Area enclosed within the mapped edges	Using calculate geometry with the attribute table of the depressions
Perimeter	P	Length of mapped edge	Using calculate geometry with the attribute table of the depressions
Circularity ratio (Rc)	Rc	Ratio between the area of the depression (A) and the area of a circle having a circumference equal to the perimeter of the depression (Miller, 1953)	$Rc = A/Ac$ Circle area given by $P^2/4\pi$
Mean elevation of perimeter	MzP	Average elevation of line that outlines the edge of the depression	(1) Transform 2D shapefile of depressions into a 3D shapefile with z values for the perimeter (3D Analyst Tools, Functional Surface, Interpolate Shape); (2) Obtain mean z value of perimeter (3D Analyst Tools, 3D Features, Add Z Information)
Volume	V	Since the edges of the depressions have a variable elevation, the approximate volume has been estimated calculating the volume of a 3D polygon defined by intersecting the surface of the depressions and a horizontal surface at an elevation given by the mean elevation of the depression perimeter (MPz).	(1) Extract DEM of areas enclosed by the depressions (Spatial Analyst Tools, Extraction, Extract by Mask). (2) Generate contour lines with 2 m interval (Spatial Analyst Tools, Surface, Contour). (3) Generate TIN (triangulated irregular network) of depressions from contour lines (3D Analyst Tools, Data Management, TIN, create TIN). (4) Calculate volume between TIN of depressions and horizontal plane at MPz elevation (3D Analyst Tools, Triangulated Surface, Polygon Volume).
Minimum elevation	Mz	Elevation of deepest point of the depression	Combining the depressions layer and the DEM, the "Zonal Statistics as Table" tool provides the minimum elevation.
Depth	D	Difference between the mean elevation of the perimeter and the elevation of deepest point	$D = MzP - Mz$
Nearest Neighbour Index	NNI	Quantifies the clustering or dispersion of depressions (centroids) within the study area	Ratio between the observed mean distance between each centroid (L_a) and its nearest neighbour and the expected mean distance for the centroids in a theoretical field with random pattern and the same density ($L_e = 0.5/\sqrt{D}$). Average Nearest Neighbour tool (Spatial Statistic Tools; Analysing Patterns)

Table 1. Code, brief definition of the morphometric parameters and spatial distribution index of the depressions and procedure used for their measurement.

Parameter	Maximum	Minimum	Average	Standard deviation
Major axis (m)	342.33	8.58	55.57	45.90
Elongation ratio	0.96	0.40	0.70	0.11
Area (m ²)	29,371.82	44.23	1,615.25	3,067.68
Perimeter (m)	1248.75	24.76	149.70	139.07
Circularity ratio	0.99	0.22	0.71	0.17
Volume (m ³)	124,515.21	0.004	3,149.42	11,213.36
Depth (m)	12.01	0.01	2.82	2.51

Table 2. Main values of the morphometric parameters derived from the close depressions inventoried in the study area.

Highlights

Closed depressions developed on equatorial layered deposits interpreted as collapse sinkholes

Detailed cartographic, morphometric and spatial-distribution analyses

Frequency-size relationships comparable with those reported for sinkholes on Earth

Possible evidence of an epigene evaporite karst

Depressions re-shaped by aeolian erosion

Journal Pre-proof

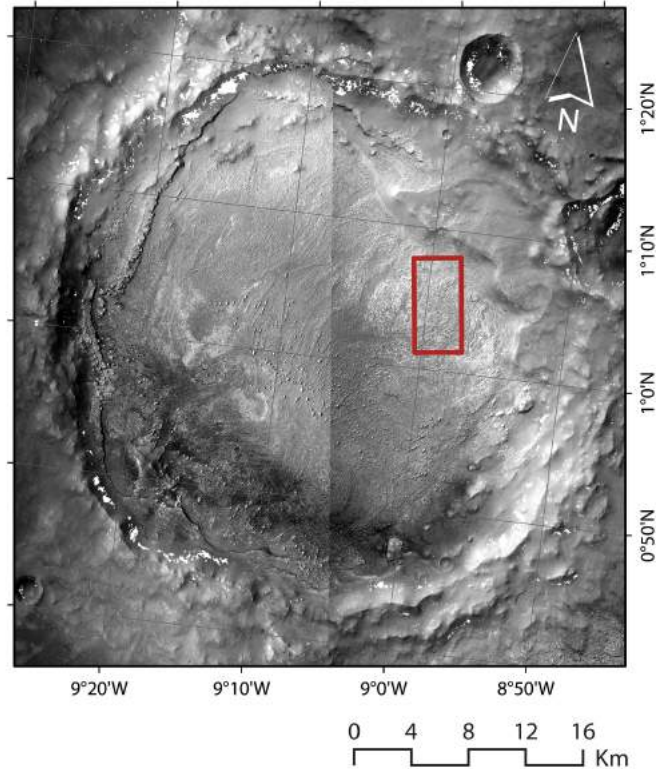
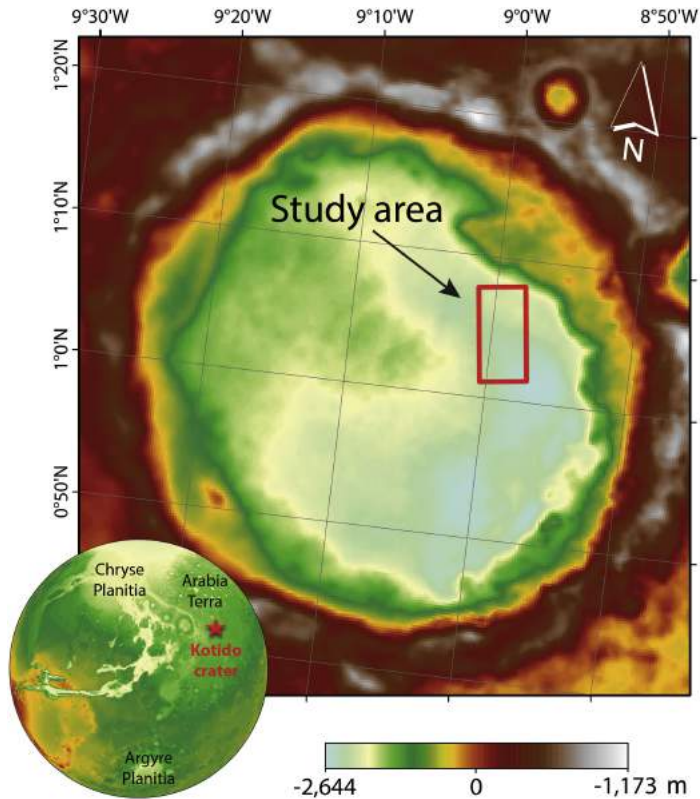


Figure 1

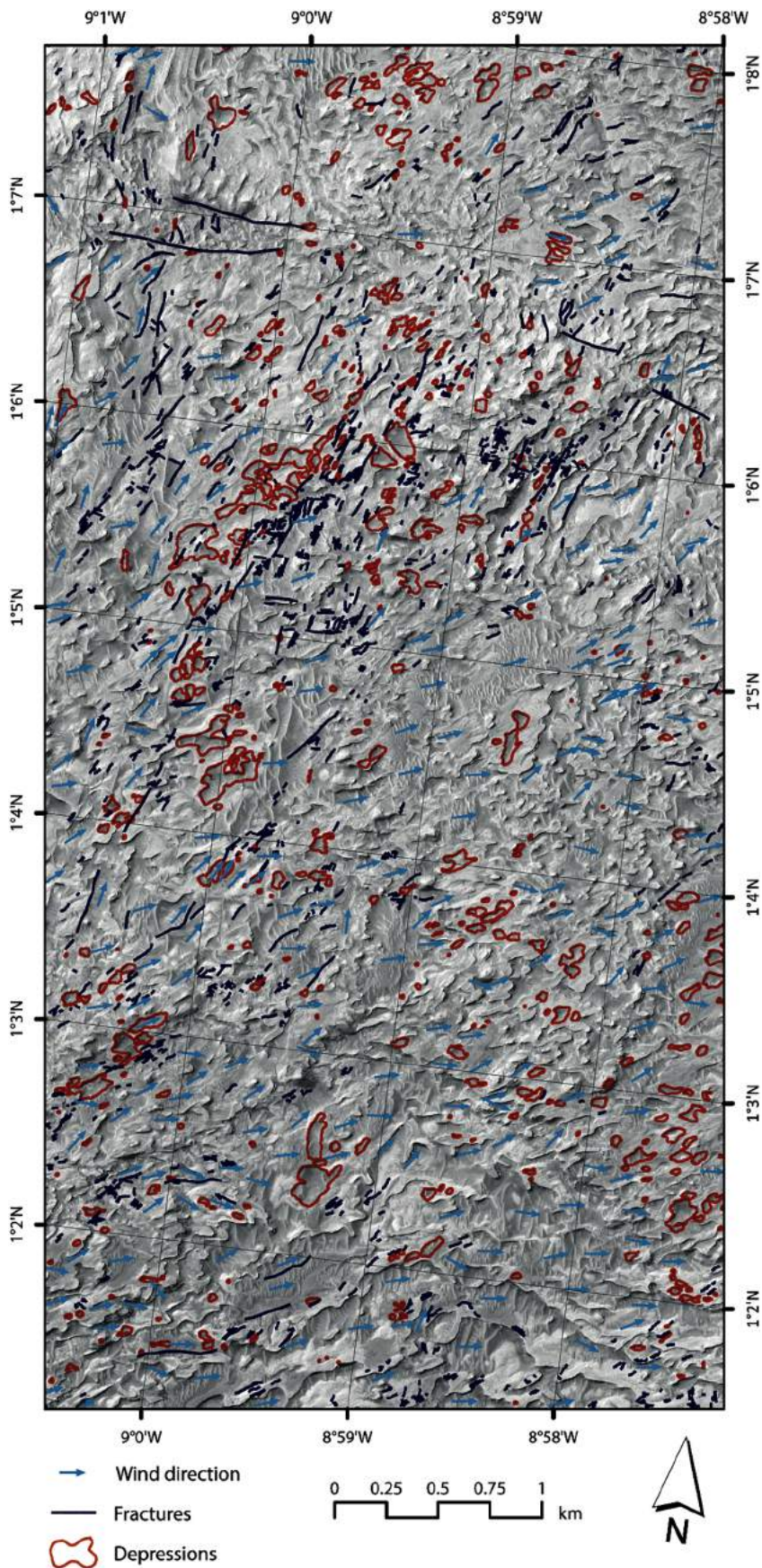


Figure 2

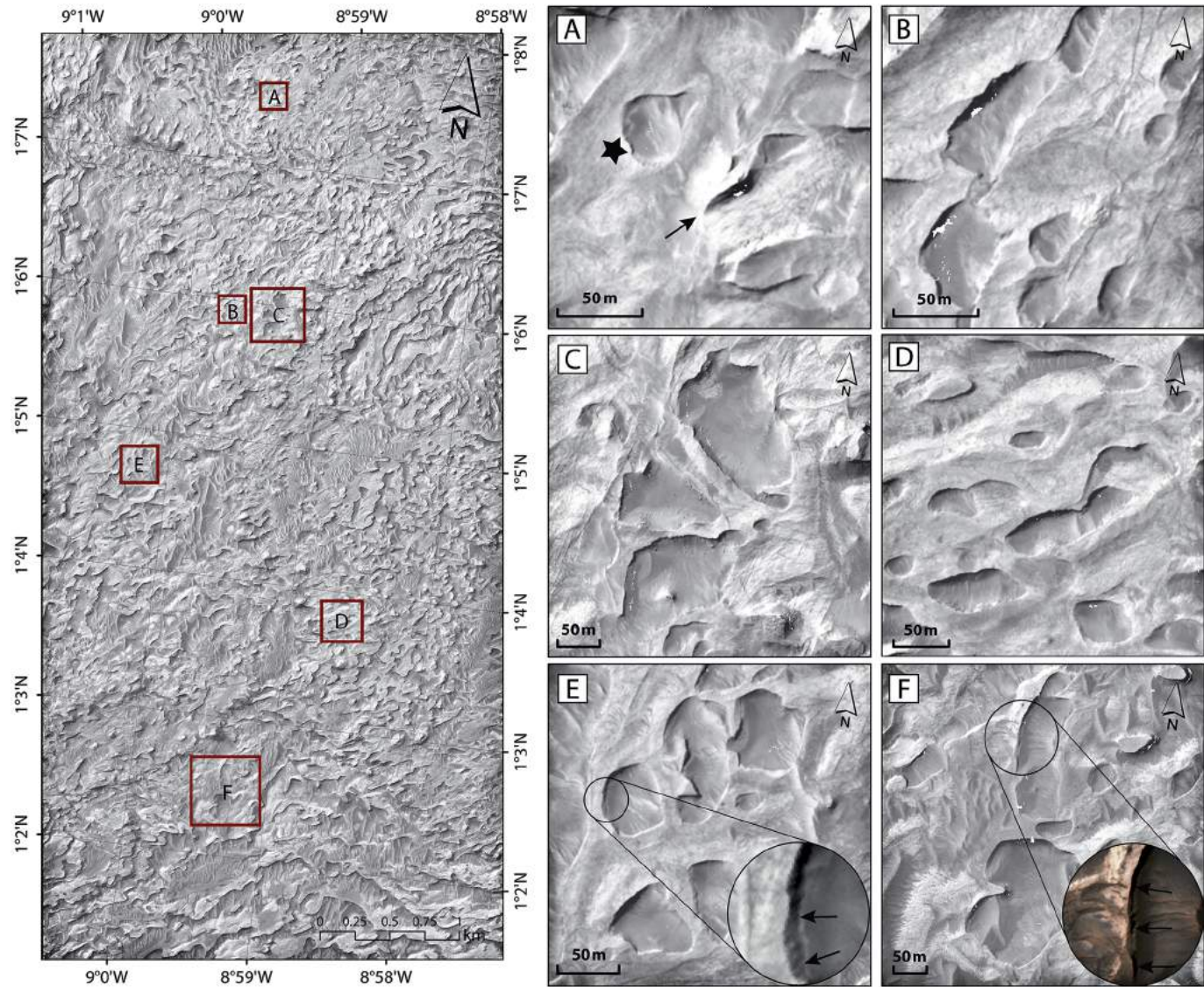


Figure 3

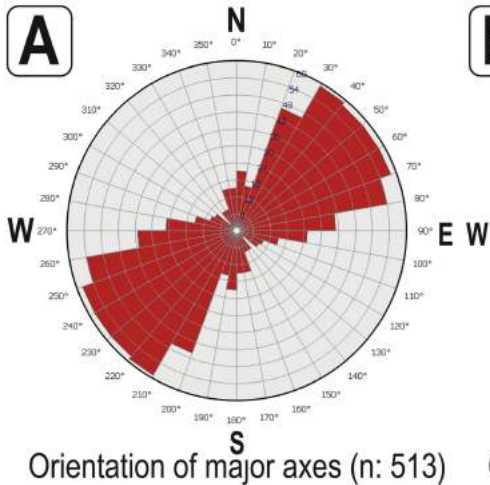
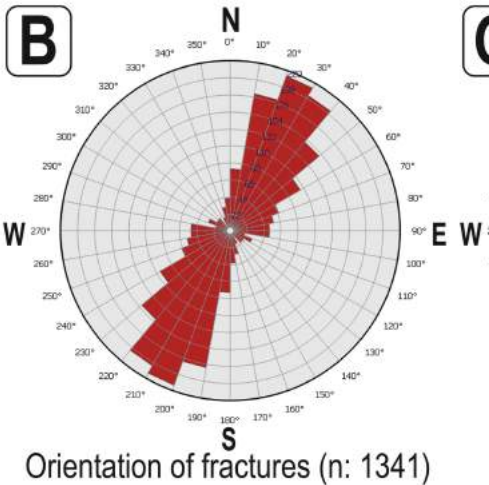
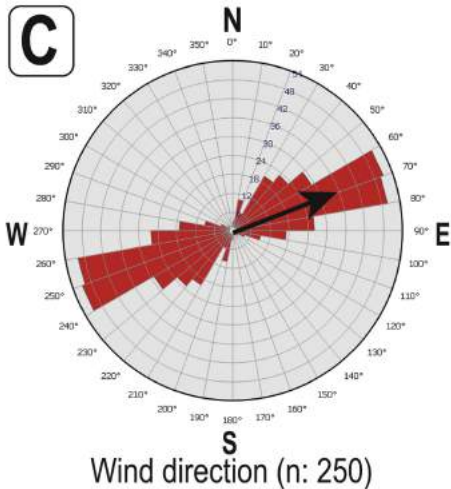
A**B****C**

Figure 4

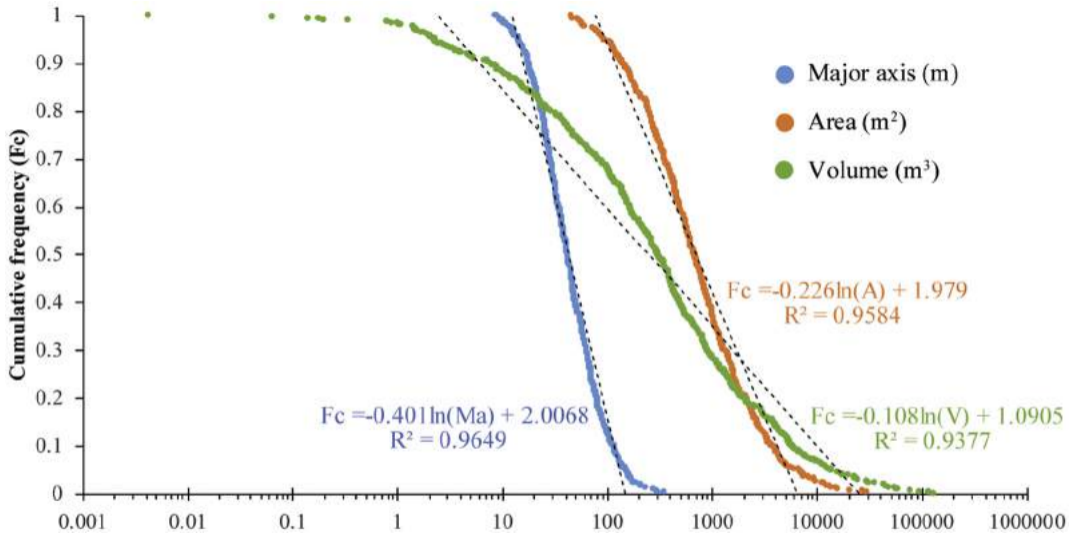
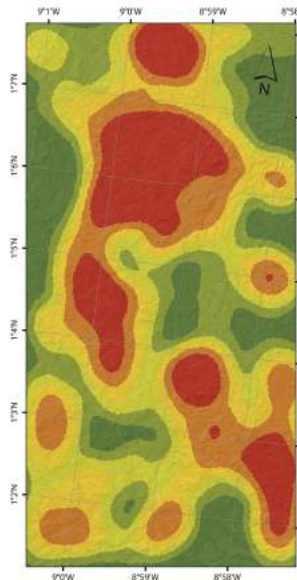
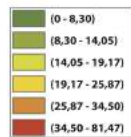


Figure 5

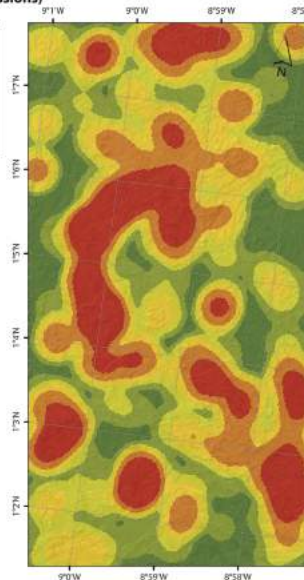
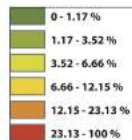
**Density map of depressions by number
(depressions/km²)**



A



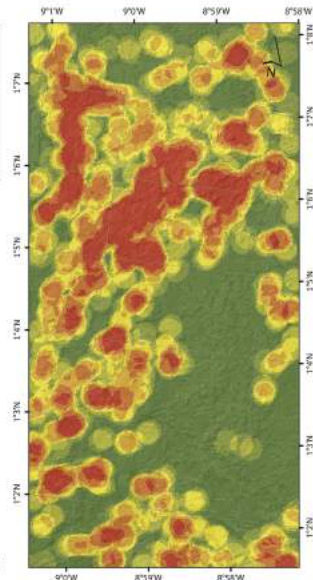
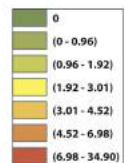
**Density map of depressions by area
(% area with depressions)**



B



**Fractures density map
(fractures/km²)**



C



Figure 6

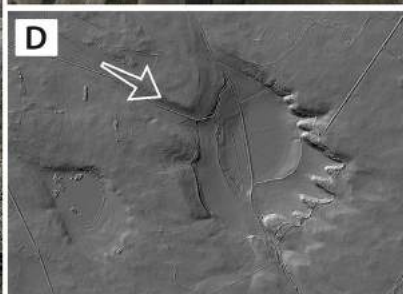


Figure 7

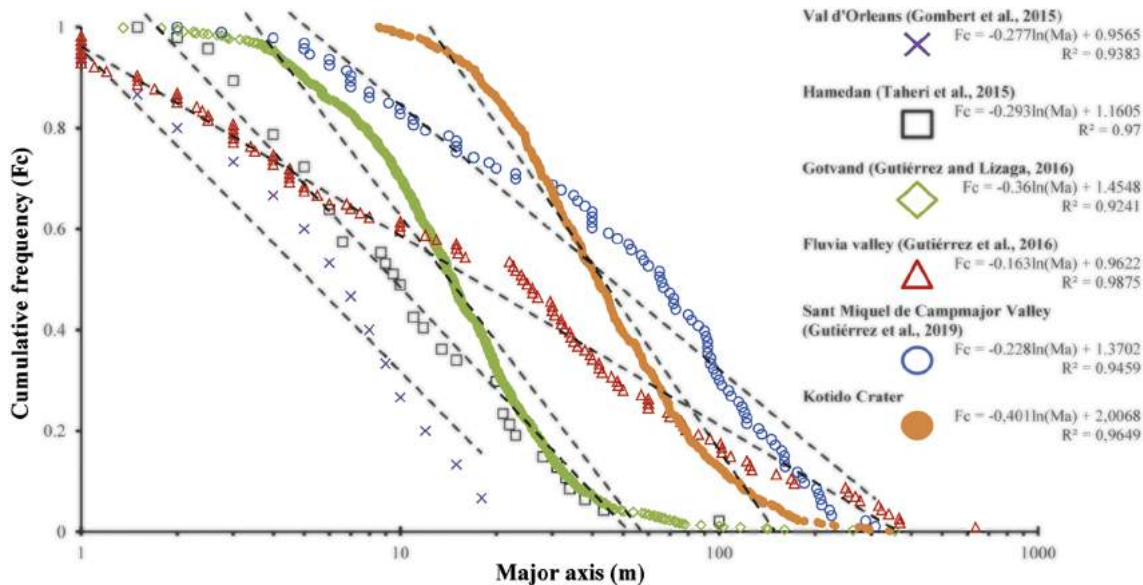


Figure 8